PCCP

Experimental and Computational Investigation of the Bond Energy of Thorium Dicarbonyl Cation and Theoretical Elucidation of Its Isomerization Mechanism to the Thermodynamically Most Stable Isomer, Thorium Oxide Ketenylidene Cation, OTh+CCO

Experimental and Computational Investigation of the Bond Energy of Thorium Dicarbonyl Cation and Theoretical Elucidation of Its Isomerization Mechanism to the Thermodynamically Most Stable Isomer, Thorium Oxide Ketenylidene Cation, OTh⁺CCO

Arjun Kafle and P. B. Armentrout*

Department of Chemistry, University of Utah, 315 S 1400 E Rm 2020, Salt Lake City, UT 84112

ABSTRACT: Collision-induced dissociation (CID) of $[Th,2C,2O]^+$ with Xe is performed using a guided ion beam tandem mass spectrometer (GIBMS). The only products observed are $ThCO^+$ and Th^+ by sequential loss of CO ligands. The experimental findings and theoretical calculations support that the structure of $[Th,2C,2O]^+$ is the bent homoleptic thorium dicarbonyl cation, $Th^+(CO)_2$, having quartet spin, which is both thermodynamically and kinetically stable enough in the gas phase to be observed in our GIBMS instrument. Analysis of the kinetic energy-dependent cross sections for this CID reaction yields the first experimental determination of the bond dissociation energy (BDE) of $(CO)Th^+\text{–}CO$ at 0 K as 1.05 ± 0.09 eV. A theoretical BDE calculated at the CCSD(T) level with cc-pVXZ (X = T and Q) basis sets and a complete basis set (CBS) extrapolation is in very good agreement with the experimental result. Although doublet spin bent thorium oxide ketenylidene cation, OTh^+CCO, is calculated to be the most thermodynamically stable structure, it is not observed in our experiment where $[Th,2C,2O]^+$ is formed by association of Th^+ and CO in a direct current discharge flow tube (DC/FT) ion source. Potential energy profiles of both quartet and doublet spin are constructed to elucidate the isomerization mechanism of $Th^+(CO)_2$ to OTh^+CCO. The failure to observe OTh^+CCO is attributed to a barrier associated with C-C bond formation, which makes OTh^+CCO kinetically inaccessible under our experimental conditions. Chemical bonding patterns in low-lying states of linear and bent $Th^+(CO)_2$ and OTh^+CCO isomers are also investigated.

INTRODUCTION

Carbon monoxide (CO) is a ubiquitous atmospheric trace gas produced by natural processes and anthropogenic pollution[1] and a critical ligand in organometallic chemistry. It can be used as a feedstock in many catalytic processes.[2] Transition metal (TM) carbonyls are frequently studied,[3-5] and the nature of the bonding in these complexes is well established, which can be explained using the Dewar-Chatt-Duncanson model.[6, 7] Here, bonds are formed by σ-donation from CO to the TM and π- back donation from the TM to the vacant degenerate π^*-orbitals of CO. TM carbonyls serve as prototypes for metal-ligand bonding in inorganic and organometallic chemistry.[8]

Unlike TM carbonyls, actinide carbonyls are less frequently studied because there are experimental challenges associated with their radioactive nature. Theoretical challenges include the need to account for many valence electrons with dense electronic states further complicated by strong relativistic and electron correlation effects. In addition, actinide experiments are complicated by several accessible oxidation states and the high reactivity of atomic actinides with O_2 and moisture.[9] For example, there are few thorium carbonyl complexes reported in the literature. $Th(CO)_n$ (n = 1–6) have been generated by reacting laser-ablated thorium atoms with CO in excess neon, where they were characterized with matrix isolation infrared (IR) spectroscopy.[10, 11] $Th^{+/-}(CO)_8$ have been studied using mass-selected IR photodissociation spectroscopy.[12] The first thermally stable thorium carbonyl complex, $[(C_5Me_5)_3Th(CO)][BPh_4]$, has been synthesized.[13] Li, Bursten, Zhou, and Andrews[11] have observed that the $Th(CO)_2$ species can undergo photochemical rearrangement to form a more thermodynamically stable species, OThCCO. Importantly, none of these studies were able to characterize the thermodynamics of any of these species. Thus, to our knowledge, neither experimental thermodynamics of $Th^{0/+}(CO)_2$ nor a detailed understanding of the mechanism for the formation of $OTh^{0/+}CCO$ from the reaction of $Th^{0/+}$ with CO has been developed.

Although mildly radioactive thorium and uranium are more frequently studied than the heavier actinides, which are dangerously radioactive, the nature of bonding in actinide complexes

in general and the role of f orbitals in bonding in actinide complexes remain to be well understood, especially from a quantitative thermochemical perspective. Understanding the nature of bonding between actinides and different ligands is vital from both a fundamental and practical perspective, as actinides are relevant to their use as nuclear fuels and the management of spent nuclear fuel. Thorium, in particular, has received renewed interest as a nuclear fuel because of the anti-proliferation properties of the thorium fuel cycle and the shorter-lived radioactive daughter products compared to the uranium fuel cycle.[14-18] Further, short-lived α emitting actinide isotopes, such as Th-227, have potential applications in cancer therapy.[19] TM carbonyl complexes have been shown to be promising in novel applications, such as in detection of nasopharyngeal carcinoma[20] or live cell imaging.[21] Therefore, a better understanding of the structure and nature of bonding in thorium carbonyls and how these vary with the number of ligands around Th could provide new insights into practical synthetic approaches of these species, their potential roles in novel applications, and further facilitate our understanding of the comparison of actinide and main group chemistry. Despite the challenges in the computational chemistry of actinide systems, computational investigations are an ideal avenue to understand the chemistry of the highly radioactive and toxic heavier actinides provided reliable experimental benchmarks, including thermodynamic information, are available to refine existing models or to develop better approaches. Accurate thermodynamic information measured from gas-phase experiments, where systems can be probed in isolation from solvent or substrate effects, can provide such benchmarks for evaluating theoretical methods. In this regard, our group has been establishing accurate experimental thermodynamic data for gas-phase actinide complexes and their comparison to high-level theory.[22-30]

Recently, we have experimentally measured the bond dissociation energy (BDE) of thorium mono-carbonyl cation, Th$^+$–CO, for the first time using a guided ion beam tandem mass spectrometer (GIBMS).[29] We complemented our experimental work by theoretical explorations of the bonding and electronic structure of different isomers of [Th,C,O],$^{0/+}$ and elucidated the mechanism for their formation and interconversion.[29] In the current study, the BDE for loss of a

CO ligand from $[Th,2C,2O]^+$ is measured by determining the kinetic energy dependence of the collision-induced dissociation (CID) of $[Th,2C,2O]^+$ with Xe, using a GIBMS. Comparison of the experimentally measured BDE with theoretical values calculated at several levels identify the structure of $[Th,2C,2O]^+$ formed in our instrument as the dicarbonyl, $Th^+(CO)_2$. In addition, potential energy profiles for the rearrangement mechanism of $Th^+(CO)_2$ in both quartet and doublet spin states are constructed to elucidate the mechanism for formation of OTh^+CCO. Chemical bonding patterns in low-lying states of linear and bent isomers of $Th^+(CO)_2$ and OTh^+CCO are also investigated.

EXPERIMENTAL AND THEORETICAL DETAILS

Experimental. Experimental methods and the GIBMS used in the present study have been described in detail previously.[31-33] Briefly, ions were generated using a direct current flow tube (DC/FT) ion source[34] containing a thorium rod cathode attached to a tantalum holder held at a negative voltage of ~1.6 kV. A gas mixture of ~90% He and 10% Ar was introduced at approximately $0.4 - 0.5$ Torr into the source chamber. Ar ions produced through the DC discharge were accelerated into the Th cathode, thereby sputtering Th^+ ions. $[Th,2C,2O]^+$ complexes were formed by introducing CO gas into the flow tube about 25 cm downstream from the discharge source. $[Th,2C,2O]^+$ complexes were swept through the remainder of a 1 m long flow tube where they underwent approximately 10^5 collisions with the He + Ar mixture, thermalizing them to 300 K. Several other systems previously studied in our lab using similar source conditions provided data consistent with the generation of the thermalized precursor molecular ions.[27, 29, 34-39] Good agreement obtained between experimental and theoretical BDEs validate this conclusion in the present system as well, see below.

Precursor ions were skimmed from the flow tube, focused, and subsequently mass-selected using a magnetic momentum analyzer. The mass-selected precursor ions were then decelerated to a desired kinetic energy and focused into a radio frequency (rf) octopole ion beam guide.[40, 41] Within the octopole, the ions passed through a static gas cell that contained the reactant gas Xe at

low pressures of 0.05 – 0.30 mTorr to ensure that the probability of multiple ion-neutral collisions is minimal. Experiments were performed at three different pressures of the Xe neutral gas, typically ~ 0.075, 0.15, and 0.30 mTorr to investigate the pressure dependence of the present system. Xe was used as the collision gas for reasons described elsewhere.[42-44] After the collision cell, the precursor and the resulting product ions drifted to the end of the octopole and were subsequently extracted, mass analyzed using a quadrupole mass filter, and their intensities were measured using a Daly detector.[45]

Measured intensities of the reactant (I_R) and product (I_P) ions were corrected for any background reactions that occur outside the collision cell. They were then converted to absolute reaction cross sections for product formation using $I_R = (I_R + I_P)exp\,(-\rho\sigma l)$, where ρ is the number density of the neutral reactant, σ is the total reaction cross section, and l is the effective length of the collision cell, 8.26 cm, as described elsewhere.[31] The uncertainty in the absolute product ion cross sections is estimated to be $\pm\,20\%$, with a relative uncertainty of $\pm\,5\%$.[41]

Ion kinetic energies in the laboratory frame energy, E_{lab}, were converted to energies in the center-of-mass frame energy, E_{CM}, by using the formula $E_{CM} = E_{lab} \times m/(m + M)$ where m and M are the masses of the Xe reactant neutral and the $[Th,2C,2O]^+$ reactant ion, respectively. E_{CM} represents the amount of energy available for inducing chemical reactions. The absolute zero of energy and kinetic energy distribution of the reactant ions were determined by using the octopole ion guide as a retarding potential analyzer.[41] The full width at half maximum was measured to be ~ 0.4 eV in the lab frame (0.13 eV CM). The absolute energy scale has an uncertainty of about 0.1 eV in the lab frame (0.03 eV CM).

CAUTION! ^{232}*Th with* $t_{1/2}$ *of 1.40 x 10^{10} years is an alpha-emitting radionuclide. All experimental work was performed following the thorium and depleted uranium handling protocol regulated by the Radiological Health Department, University of Utah (see resources at htpps://rso.utah.edu).*

Thermochemical Analysis. The kinetic-energy-dependent cross sections resulting from CID were modeled using the modified line-of-centers model shown in Eq. (1),

$$\sigma(E) = \sigma_0 \sum_i g_i(E + E_i - E_0)^N/E \qquad (1)$$

where σ_0 is an energy-independent scaling factor, E is the CM kinetic energy of the reactants, E_i is the rotational and vibrational energy of the reactants in state i having populations g_i ($\Sigma g_i = 1$), N is an adjustable parameter that describes the energy deposition function and determines the shape of the cross section,[46] and E_0 is the 0 K reaction threshold energy. The kinetic energy distributions of the reactant ion and neutral[47, 48] and the internal energies of the reactants (E_i)[34] cause broadening of the cross section. Therefore, Eq. (1) was convoluted with the kinetic energy distributions of the reactants before comparison to the experimental data.[41, 48, 49] The parameters, σ_0, N, and E_0, were optimized using a nonlinear least-squares method until they reproduced the experimental cross section.[41, 49] Because all sources of energy are accounted for in the analysis,[50] the threshold energy, E_0, obtained here is equivalent to the 0 K binding energy of a CO ligand to ThCO$^+$. Uncertainties of one standard deviation in the modeling parameters were evaluated by modeling several independent data sets using a range of reasonable N values. The uncertainty in the threshold energy also includes the absolute uncertainty in the energy scale, $\pm$ 0.03 eV (CM). In the present system, product cross sections at low energies exhibited a slight pressure dependence. Therefore, before analysis, the product cross sections were extrapolated to zero pressure, rigorously single collision conditions, eliminating any pressure effects.[51]

Quantum Chemical Calculations. All calculations reported here employed UHF-based methods and were performed using the Gaussian 09 computational software package.[52] As previously done for the Th$^+$(CO) system,[29] geometry optimization and harmonic vibrational frequency calculations of different isomers of [Th,2C,2O]$^+$ were done using B3LYP[53, 54] and BH

and HLYP (BHLYP) functionals.[55] In addition, single-point calculations of the ground state of

$Th^+(CO)_2$ were performed at the MP2[56] and coupled-cluster with single, double, and perturbative

triple excitations, CCSD(T),[57-60] methods using the B3LYP optimized geometries. Finally, the

ground state of $Th^+(CO)_2$ was optimized at the CCSD(T)/SDD/6-311+G(3df) and CCSD(T)/cc-

pVTZ levels, with zero-point energy (ZPE) corrections taken from the analogous B3LYP

calculations. These methods were chosen to make a direct comparison to our recent theoretical

results of Th^+CO,[29] which were chosen as outlined there.[29] Similar to our previous work,

exploratory lower-level calculations were performed with the Stuttgart-Dresden (SDD) valence

double-ζ, (12s11p10d8f)/[8s7p6d4f], basis set on Th that employs a quasi-relativistic small core

(60 electrons) effective core potential (ECP) (MWB)[61] obtained from the EMSL basis set

exchange[62, 63] along with the Pople[64] [6-311+G(3df)] basis sets on C and O. For brevity in the

following, this basis set will be referred to as SDD/Pople. Additional comparatively higher-level

calculations used pseudopotential (PP)-based correlation consistent polarized valence triple-ζ,

(17s16p11d10f3g1h)/[6s6p5d4f3g1h], cc-pVTZ-PP, and quadruple-ζ,

(20s17p12d11f5g3h1i)/[7s7p6d5f5g3h1i], cc-pVQZ-PP, basis sets.[65] These basis sets employ the

Stuttgart-Cologne multiconfigurational Dirac Hartree-Fock (MDF) fully relativistic small core (60

electron) ECP[66] for Th and were coupled with cc-pVTZ and cc-pVQZ basis sets for C and O

obtained from the EMSL basis set exchange.[62, 63, 67] These basis sets will be referred to as cc-pVXZ

where X = T or Q throughout the text. Using the cc-pVXZ-PP (X = T and Q) basis sets, the

complete basis set (CBS) extrapolation was performed using the Karton-Martin method,[68] Eq. (2),

for Hartree-Fock (HF) energies (where Y = 3 for T and Y = 4 for Q),

$$E_Y = E_{CBS} + A(Y + 1)e^{-6.57\sqrt{Y}} \qquad (2)$$

The CBS limit for the correlation energy was calculated using the same basis sets and Eq. (3).[69]

$$E_Y = E_{CBS} + B(Y + \frac{1}{2})^{-4} \qquad (3)$$

The use of these basis sets has previously yielded reasonable results for other $Th^{0/+}$ systems.[22, 23,

25, 26, 29, 65, 70-72] Potential energy profiles of both quartet and doublet spin were also constructed at

the B3LYP/cc-pVQZ level to elucidate the rearrangement mechanism of $Th^+(CO)_2$ to OTh^+CCO.

EXPERIMENTAL AND THEORETICAL RESULTS

Experimental Results. Typical data for the CID of $[Th,2C,2O]^+$ complexes with Xe are shown in Figure 1. Products are formed by sequential losses of CO ligands according to reactions (4) and (5).

$$[Th,2C,2O]^+ + Xe \rightarrow [Th,C,O]^+ + CO + Xe \qquad (4)$$

$$\rightarrow Th^+ + 2CO + Xe \qquad (5)$$
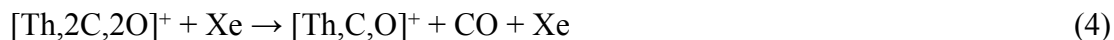
Other products such as ThO^+ and ThC^+ were explicitly looked for but not observed over the experimental energy range examined. This is reasonable if $[Th,2C,2O]^+$ is the dicarbonyl, considering the very strong C–O bond. It can be seen that the cross sections for loss of a single CO ligand from $Th^+(CO)_2$ rise from an apparent threshold near 0.5 eV and reach a plateau near 3 eV. Reaction (5) begins near 3 eV and continues to rise through the highest energies investigated. Previously, we measured $D_0(Th^+–CO)$ as 0.94 ± 0.06 eV,[29] such that the behavior seen is consistent with sequential losses of CO as the energy is increased.

Previous CID studies of TM carbonyls[34, 36, 73-75] in our group have illustrated that the primary dissociation channel provides the most accurate BDEs. Therefore, we only analyzed the cross section of reaction (4) using Eq. (1). Molecular parameters used in Eq. (1) for both reactants and products were obtained from the ground state structures located theoretically at the B3LYP/cc-pVQZ level and are given in Table S1 in the Supporting Information. The analysis assumes that there is no activation barrier in excess of the endothermicity of the dissociation process, which is typical for ion-molecule species because of the attractive long-range interactions[76] and because this is a heterolytic bond cleavage.[77] Calculated potential energy profiles confirm that no reverse activation barriers are present, see below. The cross-section model assuming a $Th^+(CO)_2$ reactant structure is shown in Figure 2 and accurately reproduces the data throughout the entire energy range examined. The average optimized parameters of Eq. (1) for multiple data sets are $\sigma_0 = 3.0 \pm 0.6$ Å^2, $N = 1.0 \pm 0.1$, and $E_0 = 1.05 \pm 0.09$ eV, where the uncertainties are one standard deviation. Alternatively, we analyzed the cross section of reaction (4) using Eq. (1) assuming a OTh^+CCO

reactant structure. Here, the optimum fitting parameters of Eq. (1) are the same as those obtained using a $Th^+(CO)_2$ reactant structure within experimental uncertainty. The experimental E_0 can be compared with theory in order to make a structural identification without any ambiguity (see below).

Theoretical Results. Several isomers of $[Th,2C,2O]^+$ were found to be stable; however, only three stable isomers of $[Th,2C,2O]^+$ are discussed in detail here, namely the thorium oxide ketenylidene cation, OTh^+CCO, and bent (C_{2v}) and linear ($D_{\infty h}$ and $C_{\infty v}$) structures of thorium dicarbonyl cation, $Th^+(CO)_2$. Note that some of the doublet states of $Th^+(CO)_2$ have significant spin contamination with $<s^2>$ values of ~ 1.75 (see Table S5) instead of a pure-spin value of 0.75, indicating considerable mixing with quartet character. Table 1 lists molecular parameters for these species along with those for the ground states of CO ($^1\Sigma^+$) and $Th^+(CO)$ ($^4\Sigma^-$) calculated using the same levels of theory used in the present work.[29] Additional isomers of $[Th,2C,2O]^+$ found along the rearrangement route of $Th^+(CO)_2$ to OTh^+CCO are discussed below.

Thorium Oxide Ketenylidene Cation, OTh^+CCO. As noted above, Li, Bursten, Zhou, and Andrews (LBZA) located the thorium oxide ketenylidene neutral in their matrix isolation study.[11] Theoretically, LBZA found this species to be the thermodynamically most stable form of $[Th,2C,2O]$ and it was formed by photolysis of thorium carbonyls. No pathways for its formation were elucidated theoretically. Molecular parameters calculated here for neutral OThCCO ($^1A'$) are in reasonable agreement with those from LBZA[11] and are given in Table S2.

Similar to the bent OThCCO neutral,[11] a bent thorium oxide ketenylidene cation, OTh^+CCO ($^2A'$), is calculated to be the lowest energy structure of $[Th,2C,2O]^+$, 1.98 eV lower than the $Th(CO)_2^+$ ground state as calculated at the B3LYP/cc-pVQZ level, Table 1. Our calculations predict a much longer Th–C bond (2.315 Å) than Th–O (1.829 Å) and a $\angle$OThC bond angle of 107°, implying the participation of 6d orbitals on the metal. The terminal CO bond length of 1.143 Å is extended from that of free CO, 1.124 Å. OTh^+CCO ($^2A'$) has a valence electron configuration of $(1a')^2(1a'')^2(2a')^2(3a')^2(4a')^1(2a'')^2$. As shown in Figure 3, the valence molecular orbitals (MOs) for OTh^+CCO ($^2A'$) are the 1a', primarily the C lone-pair electrons in CCO molecule

that σ donate to ThO⁺; the 1a″ and 2a′ are out-of-plane and in-plane Th⁺−O π bonding orbitals; the 3a′ is the Th⁺−O σ bonding orbital; and the 4a′ and 2a″ are primarily in-plane and out-of-plane CCO π orbitals, with C−C bonding but C−O antibonding character.

The OTh⁺CCO (^{4}A″) excited state is 2.39 eV higher than the global minimum isomer, OTh⁺CCO (^{2}A′), at the B3LYP/cc-pVQZ level. As shown in Table 1 and Figure S2, the electron configuration of OTh⁺CCO (^{4}A″) is similar to that of OTh⁺CCO (^{2}A′), except one 2a″ electron has been promoted to the 5a′ MO, largely 7s on Th, Figure 3. These differences result in some structural changes between the quartet and doublet spin states of OTh⁺CCO, as shown in Table 1. In OTh⁺CCO (^{4}A″), the Th–C bond length increases by 0.356 Å, the C–O bond length decreases by 0.011 Å, and the bond angle ∠OThC decreases by 16° compared to OTh⁺CCO (^{2}A′).

The electron configuration of neutral OThCCO (^{1}A′) adds a 4a′ electron to the configuration of OTh⁺CCO (^{2}A′). Compared to the ^{2}A′ state of OTh⁺CCO, the ^{1}A′ state of OThCCO has Th–C and C–C bond lengths shorter by 0.132 and 0.020 Å, respectively, and Th–O and C–O bond lengths longer by 0.048 and 0.021Å, respectively, Tables 1 and S2. The shorter Th–C and C–C bond lengths in neutral OThCCO (^{1}A′) result from more effective Th–CC π-back-bonding, consistent with the 4a′ having C−C bonding and C−O antibonding character. Interestingly, unlike the bent neutral OThCCO[11] and bent OTh⁺CCO cation calculated here, the neutral OUCCO molecule is found to prefer a linear structure.[78] This can be attributed to greater d-orbital participation in OTh$^{0/+}$CCO compared to OUCCO.

Bent Thorium Dicarbonyl Cation, Th(CO)$_2$⁺, and Its Low-Lying States. The ground state of thorium dicarbonyl cation, Th⁺(CO)$_2$, is found to be ^{4}B$_2$ with C$_{2V}$ symmetry. The formation of Th⁺(CO)$_2$ (^{4}B$_2$) can be envisioned by the addition of a CO ligand perpendicular to the ground state of Th⁺(CO) ($^4\Sigma^-$) as it has a ∠CThC bond angle of 90°. As shown in Figure 3, the valence molecular orbitals (MOs) for the bent Th⁺(CO)$_2$ isomer are the 1a$_1$ and 1b$_2$ σ bonding orbitals, where empty metal orbitals, 6d-7s hybridized and 6d, respectively, are accepting lone-pair electrons from the CO HOMOs to form σ bonds; 2a$_1$ is a metal 6d orbital π-back-bonding with in-plane CO π* MOs; 1b$_1$ and 1a$_2$ are metal 6d orbitals π-back-bonding with out-of-plane CO π*

MOs (in and out of phase); and $3a_1$ is a non-bonding MO, primarily 7s of Th. Optimized molecular parameters of the ground state of $Th^+(CO)_2$ ($^4B_2$) at the CCSD(T)/cc-pVTZ level, Table 1, with longer Th–C bonds (by 0.09 Å) and a smaller $\angle$CThC bond angle (by 11°). These differences have direct implications on the calculated BDEs discussed below. Variations in the molecular parameters of different states of $Th^+(CO)_2$ discussed below are based on results from the B3LYP/cc-pVQZ level.

The ground state of $Th(CO)_2^+$ ($^4B_2$) has a $[(1a_1)^2(1b_2)^2(2a_1)^1(1b_1)^1(1a_2)^1]$ electron configuration. Excitation of the $1a_2$ electron to the $3a_1$ MO leads to a $^4B_1$ state, 0.14 eV higher than the $^4B_2$ ground state. Our calculations predict that a $^2B_1$ state of $Th^+(CO)_2$ is the most stable among all doublet spin species of $Th^+(CO)_2$ structure, lying 0.19 eV above the $^4B_2$ ground state at the B3LYP/cc-pVQZ level. The electron configuration of the $^2B_1$ state is similar to the $^4B_2$ ground state, except the $1a_2$ electron moves to doubly occupy the $2a_1$ MO. A $^2A_1$ state lies another 0.12 eV higher and has a similar electron configuration, except the $2a_1$ is singly occupied and the $1b_1$ MO is doubly occupied, Table 1.

As shown in Table 1, compared to isolated CO, all low-lying states of bent $Th^+(CO)_2$ (C_{2V}) structure exhibit red-shifted C–O stretching frequencies, both antisymmetric (B_2 = 1957 – 1982 cm^{-1}) and symmetric (A_1 = 2014 – 2094 cm^{-1}). This indicates the presence of Th^+–CO π-back-bonding, which is consistent with our MO analysis, Figure 3. Th^+–CO back-bonding is further supported by the increase in CO bond lengths (1.136 – 1.146 Å) compared to the 1.124 Å calculated for free CO. These observations are consistent with the Dewar-Chatt-Duncanson model.[6, 7] Note that in the $^4B_1$ state, the $3a_1$ MO is a singly occupied non-bonding orbital, primarily the 7s orbital of Th^+, which may have some repulsive interaction between the central metal and CO ligands. Further, this state has only two d_π electrons involved in π-back-bonding. Consequently, this state has the longest Th^+–C (2.412 Å) and the shortest C–O (1.136 Å) bond lengths, and the least red-shifted CO stretching frequencies (B_2 = 1982 cm^{-1} and A_1 = 2094 cm^{-1}) among different low-lying states of bent $Th^+(CO)_2$. With three d_π electrons, the $^2B_1$ and $^4B_2$ states have the same C–O (1.143 Å) and similar Th^+–C (2.331 – 2.362 Å) bond lengths and have similar CO stretching

frequencies, $B_2 = 1964 - 1972$ cm^{-1} and $A_1 = 2027 - 2031$ cm^{-1}. The $^2A_1$ state has the most red-shifted C–O stretching frequencies ($B_2 = 1957$ cm^{-1} and $A_1 = 2014$ cm^{-1}), and the shortest Th$^+$–C (2.322 Å) and most extended C–O (1.146 Å) bond lengths.

We also calculated the neutral Th(CO)$_2$ ($^1A_1$) ground state at the B3LYP/cc-pVQZ level for comparison to results of LBZA[11] and our Th$^+$(CO)$_2$ ($^4B_2$) cation. The calculated and experimental (CO stretching frequencies) molecular parameters of the neutral Th(CO)$_2$ ($^1A_1$) obtained by LBZA,[11] as well as our calculated parameters are provided in Table S2. The electron configuration of neutral Th(CO)$_2$ ($^1A_1$) is similar to the Th$^+$(CO)$_2$ ($^4B_2$) cation, except the 1b$_1$ and 2a$_1$ MOs are doubly occupied, thereby emptying the 1a$_2$. Unlike in Th$^+$(CO)$_2$ ($^4B_2$), the 2a$_1$ and 3a$_1$ orbitals are more mixed in Th(CO)$_2$ ($^1A_1$). Neutral Th(CO)$_2$ ($^1A_1$) has Th–C and C–O bond lengths shorter by 0.082 Å and longer by 0.025 Å, respectively, and the ∠CThC bond angle decreases significantly by 39° compared to Th$^+$(CO)$_2$ ($^4B_2$) cation, Tables 1 and S2. These changes result from more effective Th–CO π-back-bonding in the neutral (where there are four valence electrons available compared with three for the cation), which is further enhanced by the more acute ∠CThC bond angle. The greater back bonding in neutral Th(CO)$_2$ ($^1A_1$) is further reflected in C–O stretching frequencies: LBZA[11] calculated the B$_2$ and A$_1$ CO stretches as 1734 and 1766 cm^{-1}, respectively, for Th(CO)$_2$ ($^1A_1$), whereas our calculations for neutral Th(CO)$_2$ ($^1A_1$) predict them as 1829 and 1870 cm^{-1}, respectively. Both sets of calculated values show similar magnitude shifts compared to their experimental values of 1775.6 and 1827.7 cm^{-1}, respectively.[11] CO stretching frequencies in neutral Th(CO)$_2$ ($^1A_1$) are red shifted by 143 and 161 cm^{-1} for the B$_2$ and A$_1$ modes, respectively, compared to the Th$^+$(CO)$_2$ ($^4B_2$) cation, Tables 1 and S2. These changes are consistent with previous observations that the C–O stretching frequencies of transition metal carbonyl cations and thorium monocarbonyl cation are normally higher by $100 - 200$ cm^{-1} than those of the corresponding neutrals.[5, 29]

Linear Thorium Dicarbonyl Cation, Th$^+$(CO)$_2$, and Its Low-Lying States. The most stable state of linear Th$^+$(CO)$_2$ (D$_{\infty h}$) is calculated to be $^4\Sigma_g^-$. The valence MOs for the linear Th(CO)$_2^+$ isomer are the 1σ$_g$ and 1σ$_u$ bonding MOs (where the HOMOs of both COs donate into

the empty Th^+ $6d_\sigma$ and $5f_\sigma$ orbitals); the $1\pi_g$ back-bonding MOs (where Th $6d_\pi$ electrons donate into π^* LUMOs of CO); the $2\sigma_g$ non-bonding MO (a Th $6d_\sigma$-7s hybrid orbital); the $1\pi_u$ back-bonding MO (where Th $5f_\pi$ interact with π^* LUMOs of both COs); and the $1\delta_g$ non-bonding MOs (Th $6d_\delta$ non-bonding orbitals) as shown in Figure 3.

The $^4\Sigma^-_g$ state of linear $Th^+(CO)_2$ has a $(1\sigma_g)^2(1\sigma_u)^2(1\pi_g)^2(2\sigma_g)^1$ electron configuration and lies 0.37 eV higher than the $Th^+(CO)_2$ ($^4B_2$) ground state of thorium dicarbonyl cation. The B3LYP level of theory predicts imaginary degenerate CThC bending frequencies for the $^4\Sigma_g^-$ state with all the basis sets considered in the present work (29i cm^{-1} using cc-pVQZ). At this level of theory, the molecule distorts to $Th^+(CO)_2$ ($^4B_1$) with a $\angle$CThC bond angle of 169°, only 0.004 eV higher than the $^4\Sigma_g^-$ state including zero-point energy (ZPE) corrections. Without ZPE corrections, the $^4B_1$ state lies only 0.0002 eV below the $^4\Sigma_g^-$ transition state, well below the ZPE of these states, such that the molecule is dynamically linear. Furthermore, no imaginary frequencies are present for this state at the BHLYP level of theory with all basis sets, including cc-pVQZ. Our calculations predict that a $^2\Sigma_g^-$ state is the most stable among all doublet-spin linear dicarbonyl species, lying 0.54 eV above the $^4B_2$ ground state at the B3LYP/cc-pVQZ level. The electron configuration of the $^2\Sigma_g^-$ state is the same as the $^4\Sigma_g^-$ state, except the spin of the non-bonding $2\sigma_g$ electron is flipped. Thus, the $^2\Sigma_g^-$ state has similar molecular parameters to those of the $^4\Sigma_g^-$ state, Table 1. Excitation of the $2\sigma_g$ electron to a non-bonding $1\delta_g$ orbital leads to a symmetry-broken $^4\Delta$ state with $C_{\infty v}$ symmetry (see below), which lies 0.84 eV above the $^4B_2$ ground state. Placement of three electrons in the $1\pi_g$ back-bonding MO forms a $^2\Pi_g$ $[(1\sigma_g)^2(1\sigma_u)^2(1\pi_g)^3]$ state, 0.86 eV above the ground state. A $^4\Pi_u$ state with a $[(1\sigma_g)^2(1\sigma_u)^2(1\pi_g)^2(1\pi_u)^1]$ electron configuration was also located, lies 0.94 eV above the $^4B_2$ ground state, and is formed by exciting the $2\sigma_g$ electron to the $1\pi_u$ MO. A $^2\Delta$ state has also $C_{\infty v}$ symmetry, lies 1.12 eV above the $^4B_2$ ground state and has the same electron configuration as the $^4\Delta$ state, except that the spin of the 1δ electron is flipped. A $^2\Pi_u$ state lies 1.12 eV above the $^4B_2$ ground state and has the same electron configuration as the $^4\Pi_u$ state, except that the spin of one of the $1\pi_g$ electrons is flipped. The $^2\Pi_u$ state is only 0.001 eV higher than the $^2\Delta$ state.

Similar to all low-lying states of bent $Th^+(CO)_2$ (C_{2v}), all low-lying states of linear $Th^+(CO)_2$ have red shifted C–O stretching frequencies and corresponding increases in C–O bond lengths compared to the isolated CO molecule, Table 1. $^4\Sigma_g^-$ and $^2\Sigma_g^-$ states with two π-back-bonding electrons have similar C–O (1.130 – 1.131 Å) and Th–C (2.515 – 2.521 Å) bond lengths, and similar C–O stretching frequencies, B_2 = 2058 – 2068 cm^{-1} and A_1 = 2140 – 2147 cm^{-1}, indicating the extent of π-back-bonding is similar. The $^2\Pi_g$ state with three $6d_\pi$ back-bonding electrons has the shortest Th^+–C (2.430 Å) and the longest C–O (1.141 Å) bond lengths, and the most red-shifted CO stretching frequency (B_2 = 2005 cm^{-1}) among states with only 6d orbitals of Th are involved in π-back-bonding (i.e., excluding the $^2\Pi_u$ and $^4\Pi_u$ states). Interestingly, our calculations indicate that 5f orbitals of Th may also participate in back-bonding as the red shift in CO frequencies in both the $^4\Pi_u$ $[(1\sigma_g)^2(1\sigma_u)^2(1\pi_g)^2(1\pi_u)^1]$ and $^2\Pi_u$ $[(1\sigma_g)^2(1\sigma_u)^2(1\pi_g)^2(1\pi_u)^1]$ states, where the $1\pi_u$ is a 5f based orbital of Th^+, is higher than those of states with only two $6d_\pi$ or three $6d_\pi$ back-bonding electrons, Table 1. This observation is further supported by similar Th–C (2.430 – 2.459 Å) and C–O (1.141 – 1.144 Å) bond lengths in $^4\Pi_u$, $^2\Pi_u$, and $^2\Pi_g$ states, Table 1. A similar theoretical finding was obtained for a low-lying state of thorium monocarbonyl cation.[29] Evidence of back-donation from 5f orbitals has been found by Ricks et al.[79] in $U(CO)_8^+$ and Chi et al.[12] in $An^{+/-}(CO)_8$ (An = Th, U).

Both $^4\Delta$ and $^2\Delta$ states are predicted to have asymmetric Th–C and C–O bond lengths at the B3LYP/cc-pVQZ level, Table 1. As a consequence, these states have IR active symmetric CO stretching frequencies, unlike the low-lying states of linear $Th^+(CO)_2$ with $D_{\infty h}$ symmetry. Note that similar calculations at the BHLYP/cc-pVQZ level predict a $^2\Delta_g$ state with symmetric Th–C and C–O bond lengths. These observations suggest that symmetry-broken $^4\Delta$ and $^2\Delta$ states may be a result of artifacts that skew greater charge density on one C atom or the other, as indicated in Table S3.

The bond lengths of Th–C, C–O, and CO stretching frequencies increase, decrease, and increase, respectively, when going from the ground state of $Th^+(CO)$ ($^4\Sigma^-$) to low-lying states of bent $Th^+(CO)_2$ (C_{2v}) to linear $Th^+(CO)_2$ ($D_{\infty h}$). These changes indicate there is a greater extent of

π-back-bonding in Th$^+$(CO) ($^4\Sigma^-$), followed by bent Th$^+$(CO)$_2$ (C$_{2v}$), and then linear Th$^+$(CO)$_2$ (D$_{\infty h}$). This trend follows directly from the number of π-back bonding electrons: two for the single carbonyl in Th$^+$(CO), 1.5 for each carbonyl in Th$^+$(CO)$_2$ (^{4}B$_2$), and one for each carbonyl in linear Th$^+$(CO)$_2$ ($^4\Sigma^-_g$).

Potential Energy Profiles for Rearrangement of Th$^+$(CO)$_2$ to Form the Most Stable Isomer, OTh$^+$CCO. The doublet and quartet potential energy profiles (PEPs) of [Th,2C,2O]$^+$ calculated at the B3LYP/cc-pVQZ level are shown in Figure 4, with structures along these PEPs shown in Figure 5. Energies and zero-point energies for stationary states calculated along the PEPs relative to Th$^+$(CO) ($^4\Sigma^-$) + CO ($^1\Sigma^+$), and imaginary frequencies for transition states (TSs) are listed in Table S4. The structures of most intermediates and TSs on the quartet and doublet spin PEPs are similar; however, some intermediates and TSs exist only for a particular spin state. All TSs obtained have only one imaginary frequency, and intrinsic reaction coordinate (IRC) scans were performed to verify that the TSs connect the desired intermediates.

Addition of a second CO ligand to thorium monocarbonyl cation, Th$^+$(CO), can directly form either linear Th$^+$(CO)$_2$, isomer **1**, or the bent dicarbonyl, isomer **2**. The quartet-spin linear structure, **^{4}1**, lies 0.76 eV below the Th$^+$(CO) ($^4\Sigma^-$) + CO ($^1\Sigma^+$) asymptote, whereas **^{2}1** lies 0.59 eV below this asymptote. In **TS1/2**, which connects isomers **1** and **2**, the $\angle$CThC bond angle decreases as the C–C distance between two terminal ligands decreases. Isomer **2** can convert to intermediate **3**, OCTh$^+$(η^2–CO), via **TS2/3**, where one of the $\angle$ThCO bond angles decreases as the O atom moves closer to the metal. The doublet PEP remains above the quartet through the formation of isomer **3**. Intermediate **^{4}3** can convert to planar **^{4}4**, OCTh$^+$(η^2–CO), via **^{4}TS3/4**, where the $\angle$OCThC dihedral angle changes as the C atom from one of the CO ligand moves closer to the metal and closer to the C atom of the other CO ligand by becoming planar. **^{4}5** forms from **^{4}4** via **^{4}TS4/5**, where the C–C bond length decreases. Eventually, **^{4}6** forms from **^{4}5** via **^{4}TS5/6**, where one of the Th–C bonds lengthens and the $\angle$CCO bond angle becomes closer to linear. This rearrangement is limited by **^{4}TS5/6** lying 0.48 eV above ground state reactants. Unlike the quartet spin state, **^{2}3** can convert directly to intermediate **6** via **^{2}TS3/6**, where a C–C bond is formed and

16

one Th–C bond length increases. Note that ^{2}**TS3/6** corresponds to a tight TS lying 0.32 eV above the Th$^+$(CO) ($^4\Sigma^-$) + CO ($^1\Sigma^+$) asymptote. Note that there must be crossing between the quartet and the doublet PEPs between intermediates **3** and **6**, which was not explicitly located. Finally, thorium oxide ketenylidene cation, OTh$^+$CCO, isomer **7**, forms from intermediate **6** via **TS6/7**, where one CO bond is cleaved as the ∠OThC bond angle increases and the Th–O bond length decreases.

DISCUSSION

      Comparison of Experimental and Theoretical Bond Energies. To our knowledge, no previous experimental or theoretical work on the BDE of $(CO)Th^+–CO$ has been reported to make any direct comparison to the present results. Both our experimental and calculated BDEs values are listed in Table 2. There, it can be seen that B3LYP BDEs are slightly high but lie within experimental uncertainty for all basis sets; BHLYP BDEs are slightly low but lie within experimental uncertainty except for the SDD/Pople result; MP2 single point BDEs are in good agreement with experiment except for the SDD/Pople result, which is slightly low; CCSD(T) single point BDEs are too low by $0.12 − 0.22$ eV. In agreement with the results for $ThCO^+$, CCSD(T) geometry optimizations provide better results with the SDD/Pople basis set yielding a value just outside experimental error and the cc-pVXZ results providing good reproduction of the experimental value, especially the CBS extrapolated value of 1.02 eV.

      In addition, we calculated that loss of CO from OTh^+CCO ($^2A'$), the thermodynamically most stable isomer of $[Th,2C,2O]^+$, requires 3.11 eV at the B3LYP/cc-pVQZ level of theory. (A spin-orbit corrected value obtained using a method explained in detail elsewhere[22] is 2.65 eV.) Either value is significantly higher than the experimental value of $1.05 ± 0.09$ eV. Furthermore, dissociation of OTh^+CCO ($^2A'$) to ThO^+ ($^2\Sigma^+$) + CCO ($^3\Sigma^-$) is calculated to require 3.76 eV at the B3LYP/cc-pVQZ level, which suggests that this channel should be observable at higher collision energies. As noted above, this product channel was looked for but not observed to the sensitivity level shown in Figures 1 and 2. These comparisons unambiguously indicate that the $[Th,2C,2O]^+$ species formed in our instrument is the bent homoleptic thorium dicarbonyl cation, $Th^+(CO)_2$.

      The experimental $D_0[(CO)Th^+–CO]$ value of $1.05 ± 0.09$ eV is slightly higher than $D_0(Th^+–CO) = 0.94 ± 0.06$ eV, obtained in previous GIBMS experiments.[29] In that study, the system is simple enough that geometries could be optimized at the CCSD(T) level and yielded $Th^+–CO$ BDEs of $0.87 − 0.89$ eV[29] with the cc-pVXZ (X = T and Q) basis sets and after CBS extrapolation. These values are in good agreement with experiment, and a Feller-Peterson-Dixon composite coupled-cluster value[80-83] of 0.94 eV is in excellent agreement with experiment. Here,

the CCSD(T)/CBS//CCSD(T)/cc-pVTZ results, Table 2, yield 1.02 eV for the (CO)Th$^+$–CO BDE, in very good agreement with the experimental value. Further, the calculated difference of 0.13 eV between the first and second carbonyl BDEs at this level is consistent with the experimental difference of 0.11 eV. In contrast, B3LYP, BHLYP, and MP2 levels all predict the opposite trend, by ~0.03, 0.10, and 0.11 eV, respectively. These results are consistent with previous work that found DFT methods overestimate bond energies, particularly for monocarbonyls.[84]

OTh$^+$CCO is Kinetically Inaccessible. [Th,2C,2O]$^+$ reactant complexes are formed in our DC/FT source according to the following reactions:

$$Th^+ + CO + X \quad \rightarrow ThCO^+ + X \ (X = He \ or \ Ar) \tag{6}$$

$$ThCO^+ + CO + X \rightarrow [Th,2C,2O]^+ + X \tag{7}$$
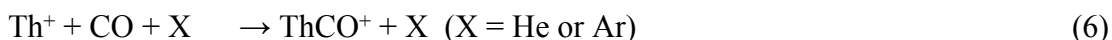
In our DC/FT source, reactant complexes are formed by sequential addition of CO ligands to the metal cation followed by 3-body stabilization and thermalization by collisions with the mixture of He and Ar gases. Such a 3-body association/stabilization mechanism suggests that the failure to generate OTh$^+$CCO isomer in our DC/FT source indicates that there must be a barrier in excess of thermal energies enroute to the OTh$^+$CCO isomer from ThCO$^+$ + CO. This conclusion is consistent with Figure 4, which shows barriers associated with the tight transition states **^{2}TS3/6** and **^{4}TS5/6**, lying 0.32 and 0.48 eV above the Th$^+$(CO) ($^4\Sigma^-$) + CO ($^1\Sigma^+$) asymptote. These barriers kinetically block the formation of OTh$^+$CCO, explaining why it is not observed under our experimental conditions.

Comparison of Sequential BDEs of M$^+$(CO)$_n$ (M= Th and Ti; n = 1 – 2). The higher BDE of (CO)Th$^+$–CO compared to Th$^+$–CO can be explained on the basis of the electronic configuration of Th in Th$^+$(CO) ($^4\Sigma^-$) and Th$^+$(CO)$_2$ (^{4}B$_2$). Our natural bond orbital (NBO) analysis[85, 86] at the B3LYP/cc-pVQZ level indicates that the valence electron configuration of Th in Th$^+$(CO) ($^4\Sigma^-$) and Th$^+$(CO)$_2$ (^{4}B$_2$) are primarily 6d^{2}7s and 6d^3, respectively, Table S3. The 7s electron in Th$^+$(CO) ($^4\Sigma^-$) is promoted to 6d in Th$^+$(CO)$_2$ (^{4}B$_2$), which allows less electronic repulsion between Th$^+$ and the HOMO of the second CO ligand, thereby increasing the bond strength in Th$^+$(CO)$_2$ (^{4}B$_2$). In addition, Th$^+$(CO)$_2$ (^{4}B$_2$) has three d$_\pi$ electrons available for π-back-

bonding compared with two in $Th^+(CO)$ ($^4\Sigma^-$); however, the π-back-bonding is distributed over two CO ligands in $Th^+(CO)_2$ ($^4B_2$). Overall, these considerations lead to higher calculated CO stretching frequencies in $Th^+(CO)_2$ ($^4B_2$) than in $Th^+(CO)$ ($^4\Sigma^-$), Table 1, but the CO bond distances are very similar. The latter suggests that the π-back-bonding is comparable in the two systems.

The J = 3/2 ground level of Th^+ is an admixture of ^4F ($6d^27s$) and ^2D ($6d7s^2$) configurations,[87] therefore, Th^+ can be compared with the group 4 transition metal cations, Ti^+ (^4F, $3d^24s$), Zr^+ (^4F, $4d^25s$), and Hf^+ (^2D, $5d6s^2$), because all have three valence electrons in s and d orbitals. Unfortunately, except for $Ti^+(CO)_n$ (n = 1 – 7), which have been measured using the same techniques as the present study,[73] experimental BDEs of the group 4 transition metal carbonyl cations are not available to make a thorough comparison. The first and second Th–CO BDEs are $D_0[(CO)Th^+{-}CO] = 1.05 \pm 0.09$ eV (this work) > $D_0[Th^+{-}CO] = 0.94 \pm 0.06$ eV,[29] whereas $D_0[(CO)Ti^+{-}CO] = 1.17 \pm 0.04$ eV < $D_0[Ti^+{-}CO] = 1.22 \pm 0.06$ eV.[73] The higher BDE of Ti^+–CO than Th^+–CO is due to different electronic ground states of $TiCO^+$ and $ThCO^+$. The ground state of $TiCO^+$ ($^4\Delta$)[88-90] and $ThCO^+$ ($^4\Sigma^-$)[29] are derived from $3d^3$ and $6d^27s$ valence configurations on M^+, respectively, with a more favorable interaction between the metal cation and CO ligand in the former. $ThCO^+$ ($^4\Sigma^-$) has repulsive interactions between the valence 7s orbital of Th^+ and the CO lone pair electrons, leading to a weaker Th^+–CO bond than the Ti^+–CO.

For the dicarbonyls, Zhou and Andrews[90] predicted the ground state of $Ti^+(CO)_2$ to be $^4B_2$. Likewise, our calculations at the B3LYP/cc-pVQZ(Ti)/cc-pVQZ (C,O) level predict the bent $Ti^+(CO)_2$ ($^4B_2$) as the ground state as well, with a $3d^3$ valence electron configuration on Ti^+. Therefore, the lower BDE of $(CO)Ti^+$–CO than Ti^+–CO can be explained on the basis of reduced π-back-bonding and increased ligand-ligand repulsion in $Ti^+(CO)_2$ ($^4B_2$)[90] compared to $Ti^+(CO)$ ($^4\Delta$).[88-90] Likewise, the higher BDE of $(CO)Ti^+$–CO compared to $(CO)Th^+$–CO can be understood on the basis of the promotion energy needed to achieve a d^3 valence electronic configuration (needed to effectively interact with the π^* LUMOs of COs) from the ground state electronic configuration of M^+. The ^4F ($3d^3$) excited state of Ti^+ lies only 0.11 eV[87] higher than the ^4F ($3d^24s$) ground state. In contrast, the ^4F ($6d^3$) state of Th^+ lies much higher in energy, 0.97 eV above the

[2]D ground state,[29] or alternatively, the lowest J=3/2 level with a $6d^3$ configuration of Th^+ lies 0.87 eV above the J = 3/2 ground level.[87] Additional factors such as the difference in atomic radius of M^+, and the delicate balance of σ and π-back-bonding in M^+–CO may also influence the differences in the carbonyl BDEs of Ti^+ and Th^+.

SUMMARY

Collision-induced dissociation of $[Th,2C,2O]^+$ with Xe forms only $ThCO^+$ and Th^+. Comparing the E_0 obtained from analysis of the $Th^+(CO)$ product cross section using Eq. 1 to the theoretical values unambiguously determines that the $[Th,2C,2O]^+$ species formed in our instrument is the bent homoleptic thorium dicarbonyl cation, $Th^+(CO)_2$. The $D_0[(CO)Th^+–CO]$ bond energy is experimentally measured for the first time as 1.05 ± 0.09 eV. The calculated BDEs of $(CO)Th^+$–CO at the CCSD(T)/CBS level of theory is in excellent agreement with the experimental result. $Th^+(CO)_2$ ($^4B_2$) is not the lowest energy isomer of $[Th,2C,2O]^+$, but it is easily formed by addition of CO to the thorium monocarbonyl cation, $Th^+(CO)$ ($^4\Sigma^-$). A barrier (**^{2}TS3/6**) enroute to the formation of the thermodynamically most stable isomer, doublet-spin bent thorium oxide ketenylidene cation, OTh^+CCO ($^2A'$), kinetically blocks its formation, explaining why it is not observed experimentally. Given the relatively low barrier (0.32 eV at the B3LYP/cc-pVQZ level) for formation of this species, it seems feasible that this C–C coupling reaction could occur under different experimental conditions than the rapid thermalizations inherent in the present experiments. C–C triple bond formation usually occurs via coupling reactions at high temperatures,[91] whereas the theoretical results presented here indicate a strongly exothermic process (partially driven by formation of the strong Th–O bond). Thus, the present theoretical results may provide new insights into viable routes for C–C coupling reactions.

$D_0[(CO)Th^+–CO)]$ is smaller than its transition metal cation congener, Ti^+. The lower BDE of $(CO)Th^+$–CO compared to $(CO)Ti^+$–CO is primarily explained on the basis of the much higher promotion energy for Th^+ compared to Ti^+ needed to achieve a d^3 valence electronic configuration, which is needed in order to have favorable interactions between M^+ and CO ligands.

ASSOCIATED CONTENT

Supplementary Information

This material is available free of charge at https://pubs.rsc.org. Table S1 shows vibrational frequencies and rotational constants of CO ($^1\Sigma^+$), Th$^+$(CO) ($^4\Sigma^-$), and Th$^+$(CO)$_2$ ($^4B_2$) calculated at the B3LYP/cc-pVQZ level. Table S2 provides the molecular parameters of ground states of neutral Th(CO)$_2$ ($^1A_1$) and OThCCO ($^1A'$) calculated at the B3LYP/cc-pVQZ level (this work) compared to literature information from ref. 11. Table S3 gives natural charges on C, O, and Th, and valence electron configuration of Th in low-lying states of Th$^+$(CO)$_2$ (C$_{2v}$, D$_{\infty h}$ and C$_{2v}$) obtained from an NBO analysis conducted at the B3LYP/cc-pVQZ level; Table S4 gives energies and zero-point energies for transition states (and their imaginary frequencies) and intermediates calculated along the potential energy profiles of [Th,2C,2O]$^+$ for the formation of OTh$^+$CCO calculated at the B3LYP/cc-pVQZ level. Table S5 gives the energies and zero-point energies of CO, Th$^+$CO, and different isomers of [Th,2C,2O]$^+$ calculated at different levels of theory with SDD/6-311+G(3df) and cc-pVXZ-PP (X = T and Q) basis sets. Figure S1 shows structures of different isomers of [Th,2C,2O]$^+$ and their relative energies in eV with respect to the Th$^+$(CO)$_2$ ($^4B_2$) state calculated at the B3LYP/cc-pVQZ level. Figure S2 shows the MOs of OTh$^+$CCO ($^4A''$).

AUTHOR INFORMATION

Corresponding Author
E-mail: armentrout@chem.utah.edu

ORCID

P. B. Armentrout: 0000-0003-2953-6039

A. Kafle: 0000-0003-0792-6255

Notes

The authors declare no competing financial interest.

22

REFERENCES

1. P. R. F. Cordero, K. Bayly and P. Man Leung, *ISME J.*, 2019, **13**, 2868 − 2881.

2. J.-B. Peng, H.-Q. Geng and X.-F. Wu, *Chem*, 2019, **5**, 526 − 552.

3. G. Frenking, I. Fernández, N. Holzmann, S. Pan, I. Krossing and M. Zhou, *JACS Au*, 2021, **1**, 623 − 645.

4. A. M. Ricks, Z. E. Reed and M. A. Duncan, *J. Mol. Spectrosc.*, 2011, **266**, 63 − 74.

5. M. Zhou, L. Andrews and C. W. Bauschlicher, *Chem. Rev.*, 2001, **101**, 1931 − 1962.

6. M. J. S. Dewar, *Bull. Soc. Chim. Fr.*, 1951, **18**, C71 − C79.

7. J. Chatt and L. A. Duncanson, *J.Chem.Soc.*, 1953, 2939 − 2947.

8. J. E. Huheey, E. A. Keiter and R. L. Keiter, *Inorganic Chemistry : Principles of Structure and Reactivity*, HarperCollins, New York, 1993.

9. A. Kovács, R. J. M. Konings, J. K. Gibson, I. Infante and L. Gagliardi, *Chem. Rev.*, 2015, **115**, 1725 − 1759.

10. M. Zhou, L. Andrews, J. Li and B. E. Bursten, *J. Am. Chem. Soc.*, 1999, **121**, 12188 − 12189.

11. J. Li, B. E. Bursten, M. Zhou and L. Andrews, *Inorg. Chem.*, 2001, **40**, 5448 − 5460.

12. C. Chi, S. Pan, J. Jin, L. Meng, M. Luo, L. Zhao, M. Zhou and G. Frenking, *Chem. Eur. J.*, 2019, **25**, 11772 − 11784.

13. R. R. Langeslay, G. P. Chen, C. J. Windorff, A. K. Chan, J. W. Ziller, F. Furche and W. J. Evans, *J. Am. Chem. Soc.*, 2017, **139**, 3387 − 3398.

14. IAEA, *Thorium Fuel Cycle - Potential Benefits and Challenges*, Report IAEA-TECDOC-1450, International Atomic Energy Agency (IAEA), Vienna, Austria, 2005.

15.   C. Lombardi, L. Luzzi, E. Padovani and F. Vettraino, *Prog. Nucl. Energy*, 2008, **50**, 944 − 953.

16.   M. B. Schaffer, *Energy Policy*, 2013, **60**, 4 − 12.

17.   M. Lung and O. Gremm, *Nucl. Eng. Des.*, 1998, **180**, 133 − 146.

18.   K. M. Bae and M. H. Kim, *Nucl. Eng. Technol.*, 2005, **37**, 91 − 100.

19.   R. Eychenne, M. Chérel, F. Haddad, F. Guérard and J.-F. Gestin, *Pharmaceutics*, 2021, **13**.

20.   D. Lin, C.-L. Hsieh, K.-C. Hsu, P.-H. Liao, S. Qiu, T. Gong, K.-T. Yong, S. Feng and K. V. Kong, *Nature Communications*, 2021, **12**, 3430.

21.   K. V. Kong, Z. Lam, W. D. Goh, W. K. Leong and M. Olivo, *Angewandte Chemie (International ed. in English)*, 2012, **51**, 9796 − 9799.

22.   R. M. Cox, P. B. Armentrout and W. A. de Jong, *Inorg. Chem.*, 2015, **54**, 3584 − 3599.

23.   R. M. Cox, M. Citir, P. B. Armentrout, S. R. Battey and K. A. Peterson, *J. Chem. Phys.*, 2016, **144**, 184 − 309.

24.   R. M. Cox and P. B. Armentrout, *J. Am. Soc. Mass Spectrom.*, 2019.

25.   R. M. Cox, A. Kafle, P. B. Armentrout and K. A. Peterson, *J. Chem. Phys.*, 2019, **151**, 034304.

26.   A. Kafle, C. Nwokolo, L. Sanchez and P. B. Armentrout, *J. Phys. Chem. A*, 2020, **124**, 3090 − 3100.

27.   P. B. Armentrout and K. A. Peterson, *Inorg. Chem.*, 2020, **59**, 3118 − 3131.

28.   A. Kafle and P. B. Armentrout, *J. Phys. Chem. A*, 2019, **123**, 5893 − 5905.

29.   A. Kafle, P. B. Armentrout, S. R. Battey and K. A. Peterson, *Inorg. Chem.*, 2021, **60**, 10426 − 10438.

30.   W.-J. Zhang, M. Demireva, J. Kim, W. A. de Jong and P. B. Armentrout, *J. Phys. Chem. A*, 2021, **125**, 7825 − 7839.

31.   S. K. Loh, D. A. Hales, L. Lian and P. B. Armentrout, *J. Chem. Phys.*, 1989, **90**, 5466 − 5485.

32.   P. B. Armentrout, *J. Am. Soc. Mass Spectrom.*, 2002, **13**, 419 − 434.

33.   P. B. Armentrout, *Int. J. Mass Spectrom.*, 2000, **200**, 219 − 241.

34.   R. H. Schultz and P. B. Armentrout, *Int. J. Mass Spectrom. Ion Processes*, 1991, **107**, 29 − 48.

35.   C. S. Hinton, M. Citir, M. Manard and P. B. Armentrout, *Int. J. Mass Spectrom.*, 2011, **308**, 265 − 274.

36.   F. A. Khan, D. E. Clemmer, R. H. Schultz and P. B. Armentrout, *J. Phys. Chem.*, 1993, **97**, 7978 − 7987.

37.   R. H. Schultz, K. C. Crellin and P. B. Armentrout, *J. Am. Chem. Soc.*, 1991, **113**, 8590 − 8601.

38.   D. E. Clemmer, N. Aristov and P. B. Armentrout, *J. Phys. Chem.*, 1993, **97**, 544 − 552.

39.   D. E. Clemmer, Y.-M. Chen, F. A. Khan and P. B. Armentrout, *J. Phys. Chem.*, 1994, **98**, 6522 − 6529.

40.   E. Teloy and D. Gerlich, *Chem. Phys.*, 1974, **4**, 417 − 427.

41.   K. M. Ervin and P. B. Armentrout, *J. Chem. Phys.*, 1985, **83**, 166 − 189.

42.   N. Aristov and P. B. Armentrout, *J. Phys. Chem.*, 1986, **90**, 5135 − 5140.

43.   N. F. Dalleska, K. Honma, L. S. Sunderlin and P. B. Armentrout, *J. Am. Chem. Soc.*, 1994, **116**, 3519 − 3528.

44.   D. A. Hales and P. B. Armentrout, *J. Clust. Sci.*, 1990, **1**, 127 − 142.

45.   N. R. Daly, *Rev. Sci. Instrum.*, 1960, **31**, 264 − 267.

46.   F. Muntean and P. B. Armentrout, *J. Chem. Phys.*, 2001, **115**, 1213 − 1228.

47.   P. J. Chantry, *J. Chem. Phys.*, 1971, **55**, 2746 − 2759.

48.   C. Lifshitz, R. L. C. Wu, T. O. Tiernan and D. T. Terwilliger, *J. Chem. Phys.*, 1978, **68**, 247 − 260.

49.   N. Aristov and P. B. Armentrout, *J. Am. Chem. Soc.*, 1986, **108**, 1806 − 1819.

50.   N. F. Dalleska, K. Honma and P. B. Armentrout, *J. Am. Chem. Soc.*, 1993, **115**, 12125 − 12131.

51.   D. A. Hales, L. Lian and P. B. Armentrout, *Int. J. Mass Spectrom. Ion Processes*, 1990, **102**, 269 − 301.

52.   M. J. Frisch, G. W. Trucks, H. B. Schlegel, G. E. Scuseria, M. A. Robb, J. R. Cheeseman, G. Scalmani, V. Barone, B. Mennucci, G. A. Petersson, H. Nakatsuji, M. Caricato, X. Li, H. P. Hratchian, A. F. Izmaylov, J. Bloino, G. Zheng, J. L. Sonnenberg, M. Hada, M. Ehara, K. Toyota, R. Fukuda, J. Hasegawa, M. Ishida, T. Nakajima, Y. Honda, O. Kitao,

H. Nakai, T. Vreven, J. A. Montgomery, Jr., J. E. Peralta, F. Ogliaro, M. Bearpark, J. J. Heyd, E. Brothers, K. N. Kudin, V. N. Staroverov, R. Kobayashi, J. Normand, K. Raghavachari, A. Rendell, J. C. Burant, S. S. Iyengar, J. Tomasi, M. Cossi, N. Rega, N. J. Millam, M. Klene, J. E. Knox, J. B. Cross, V. Bakken, C. Adamo, J. Jaramillo, R. Gomperts, R. E. Stratmann, O. Yazyev, A. J. Austin, R. Cammi, C. Pomelli, J. W. Ochterski, R. L. Martin, K. Morokuma, V. G. Zakrzewski, G. A. Voth, P. Salvador, J. J. Dannenberg, S. Dapprich, A. D. Daniels, O. Farkas, J. B. Foresman, J. V. Ortiz, J. Cioslowski and D. J. Fox, Gaussian Inc., Pittsburgh, PA, Gaussian 09, Revision A.02 edn., 2009.

53.   A. D. Becke, *J. Chem. Phys.*, 1993, **98**, 5648 − 5652.

54.   C. Lee, W. Yang and R. G. Parr, *Phys. Rev. B*, 1988, **37**, 785 − 789.

55.   A. D. Becke, *J. Chem. Phys.*, 1993, **98**, 1372 − 1377.

56.   C. Möller and M. S. Plesset, *Phys. Rev.*, 1934, **46**, 618 − 622.

57.   G. D. Purvis and R. J. Bartlett, *J. Chem. Phys.*, 1982, **76**, 1910 − 1918.

58.   J. A. Pople, M. Head-Gordon and K. Raghavachari, *J. Chem. Phys.*, 1987, **87**, 5968 − 5975.

59.   G. E. Scuseria, C. L. Janssen and H. F. Schaefer, *J. Chem. Phys.*, 1988, **89**, 7382 − 7387.

60.   G. E. Scuseria and H. F. Schaefer, *J. Chem. Phys.*, 1989, **90**, 3700 − 3703.

61.   W. Küchle, M. Dolg, H. Stoll and H. Preuss, *J. Chem. Phys.*, 1994, **100**, 7535 − 7542.

62.   K. L. Schuchardt, B. T. Didier, T. Elsethagen, L. Sun, V. Gurumoorthi, J. Chase, J. Li and T. L. Windus, *J. Chem. Inf. Model.*, 2007, **47**, 1045 − 1052.

63.   D. Feller, *J. Comput. Chem.*, 1996, **17**, 1571 − 1586.

64.   R. Krishnan, J. S. Binkley, R. Seeger and J. A. Pople, *J. Chem. Phys.*, 1980, **72**, 650 − 654.

65.   K. A. Peterson, *J. Chem. Phys.*, 2015, **142**, 074105.

66.   A. Weigand, X. Cao, T. Hangele and M. Dolg, *J. Phys. Chem. A.*, 2014, **118**, 2519 − 2530.

67.   T. H. Dunning, *J. Chem. Phys.*, 1989, **90**, 1007 − 1023.

68.   A. Karton and J. M. L. Martin, *Theor. Chem. Acct.*, 2006, **115**, 330 − 333.

69.   J. M. L. Martin, *Chem. Phys. Lett.*, 1996, **259**, 669 − 678.

70.   L. Andrews, Y. Gong, B. Liang, V. E. Jackson, R. Flamerich, S. Li and D. A. Dixon, *J. Phys. Chem. A*, 2011, **115**, 14407 − 14416.

71.   L. Andrews, K. S. Thanthiriwatte, X. Wang and D. A. Dixon, *Inorg. Chem.*, 2013, **52**, 8228 − 8233.

72.   K. S. Thanthiriwatte, X. Wang, L. Andrews, D. A. Dixon, J. Metzger, T. Vent-Schmidt and S. Riedel, *J. Phys. Chem. A*, 2014, **118**, 2107 − 2119.

73.   F. Meyer and P. B. Armentrout, *Mol. Phys*, 1996, **88**, 187 − 197.

74.   F. Meyer, Y.-M. Chen and P. B. Armentrout, *J. Am. Chem. Soc.*, 1995, **117**, 4071 − 4081.

75.   M. R. Sievers and P. B. Armentrout, *J. Phys. Chem.*, 1995, **99**, 8135 − 8141.

76.   V. L. Talrose, P. S. Vinogradov and I. K. Larin, in *Gas Phase Ion Chemistry*, ed. M. T. Bowers, Academic, New York1979, vol. 1, pp. 305 − 347.

77.   P. B. Armentrout and J. Simons, *J. Am. Chem. Soc.*, 1992, **114**, 8627 − 8633.

78.   M. Zhou, L. Andrews, J. Li and B. E. Bursten, *J. Am. Chem. Soc.*, 1999, **121**, 9712 − 9721.

79.   A. M. Ricks, L. Gagliardi and M. A. Duncan, *J. Am. Chem. Soc.* , 2010, **132**, 15905 − 15907.

80.   D. A. Dixon, D. Feller and K. A. Peterson, in *Annual Reports in Computational Chemistry*, ed. R. A. Wheeler, Elsevier2012, vol. 8, pp. 1 − 28.

81.   D. Feller, K. A. Peterson and D. A. Dixon, *J. Chem. Phys.*, 2008, **129**, 204105.

82.   K. A. Peterson, D. Feller and D. A. Dixon, *Theor. Chem. Acc.*, 2012, **131**, 1079.

83.   D. Feller, K. A. Peterson and D. A. Dixon, *Mol. Phys.*, 2012, **110**, 2381 − 2399.

84.   A. J. Lupinetti, V. Jonas, W. Thiel, S. H. Strauss and G. Frenking, *Chem.Eur. J.*, 1999, **5**, 2573 − 2583.

85.   J. P. Foster and F. Weinhold, *J. Am. Chem. Soc.* , 1980, **102**, 7211 − 7218.

86.   E. D. Glendening, A. E. Reed, J. E. Carpenter and F. Weinhold, 2003.

87.   A. Kramida and Y. Ralchenko, J. Reader and NIST ASD Team, *NIST Atomic Spectra Database (version 5.8)*, National Institute of Standards and Technology, Gaithersburg, MD, 2020, avaialable online https://physics.nist.gov/asd, accessed January 17 2021.

88.   C. W. Bauschlicher and L. A. Barnes, *Chem. Phys.*, 1988, **124**, 383 − 394.

89.   L. A. Barnes, M. Rosi and C. W. Bauschlicher, *J. Chem. Phys.*, 1990, **93**, 609 − 624.

90.   M. Zhou and L. Andrews, *J. Phys. Chem. A*, 1999, **103**, 5259 – 5268.

91.   A. Bino, M. Ardon and E. Shirman, *Science*, 2005, **308**, 234−235.

Table 1. Bond lengths (r), bond angles (∠), vibrational frequencies (ω_e), and relative energies of low-lying states of [Th,2C,2O]$^+$, and ground states of Th$^+$(CO) and CO calculated at the B3LYP/cc-pVQZ level except as specified.

Species	State	Electron Configuration [a]	r (Å)		∠CThC or∠OThC (°)	ω_e (cm^{-1}) C–O stretch		E$_{rel}$ (eV) [b]
			Th–C	C–O		antisymm.	symm.	
Th$^+$(CO)$_2$ (C$_{2v}$)[c]	^{4}B$_2$	(1a$_1$)^2(1b$_2$)^2(2a$_1$)^1(1b$_1$)^1(1a$_2$)^1	**2.450**	**1.144**	**79**			0.00
Th$^+$(CO)$_2$ (C$_{2v}$)	^{4}B$_2$	(1a$_1$)^2(1b$_2$)^2(2a$_1$)^1(1b$_1$)^1(1a$_2$)^1	2.362	1.143	90	1972	2031	0.00
	^{4}B$_1$	(1a$_1$)^2(1b$_2$)^2(2a$_1$)^1(1b$_1$)^1(3a$_1$)^1	2.412	1.136	66	1982	2094	0.14
	^{2}B$_1$	(1a$_1$)^2(1b$_2$)^2(2a$_1$)^2(1b$_1$)^1	2.331	1.143	64	1964	2027	0.19
	^{2}A$_1$	(1a$_1$)^2(1b$_2$)^2(2a$_1$)^1(1b$_1$)^2	2.322	1.146	60	1957	2014	0.31
	^{4}B$_1$	(1a$_1$)^2(1b$_2$)^2(1a$_2$)^1(2b$_2$)^1(2a$_1$)^1	2.515	1.131	169	2062	2129	0.37
Th$^+$(CO)$_2$ (D$_{\infty h}$)	$^4\Sigma_g^-$	(1σ_g)^2(1σ_u)^2(1π_g)^2(2σ_g)^1	2.521	1.130	180	2068	2147	0.37
	$^2\Sigma_g^-$	(1σ_g)^2(1σ_u)^2(1π_g)^2(2σ_g)^1	2.515	1.131	180	2058	2140	0.54
Th$^+$(CO)$_2$ (C$_{\infty v}$) [d]	$^4\Delta$	(1σ)^2(1σ)^2(1π)^2(1δ)^1	2.498, 2.595	1.135, 1.128	180	2034	2143 [e]	0.84
Th$^+$(CO)$_2$ (D$_{\infty h}$)	$^2\Pi_g$	(1σ_g)^2(1σ_u)^2(1π_g)^3	2.430	1.141	180	2005	2067	0.86
	$^4\Pi_u$	(1σ_g)^2(1σ_u)^2(1π_g)^2(1π_u)^1	2.455	1.144	180	1979	2032	0.94
Th$^+$(CO)$_2$ (C$_{\infty v}$) [d]	$^2\Delta$	(1σ)^2(1σ)^2(1π)^2(1δ)^1	2.519, 2.546	1.134, 1.132	180	2015	2126 [e]	1.12
Th$^+$(CO)$_2$ (D$_{\infty h}$)	$^2\Pi_u$	(1σ_g)^2(1σ_u)^2(1π_g)^2(1π_u)^1	2.459	1.144	180	1982	2034	1.12
OTh$^+$CCO (C$_s$)[f]	^{2}A'	(1a')^2(1a")^2(2a')^2(3a')^2(4a')^1(2a")^2	2.315	1.154	107		2080	-1.98
	^{4}A"	(1a')^2(1a")^2(2a')^2(3a')^2(4a')^1(2a")^1(5a')^1	2.671	1.143	91		2089	0.41
Th$^+$(CO) (C$_{\infty v}$)	$^4\Sigma^-$	1σ^2 1π^2 2σ^1	2.274	1.149			1953	
CO (C$_{\infty v}$)	$^1\Sigma^+$			1.124			2214	

[a] Orbitals can be found in Figure 3. [b] Relative energies calculated with respect to the experimentally observed Th$^+$(CO)$_2$ (^{4}B$_2$). [c] Optimized molecular parameters of the ^{4}B$_2$ ground state of Th$^+$(CO)$_2$ calculated at the CCSD(T)/cc-pVTZ level are shown in bold. [d] Symmetry-broken states (as discussed in the text). [e] IR active. [f] Additional molecular parameters are given in Figure 5.

Table 2. Comparison of theoretical Th$^+$–CO and (CO)Th$^+$–CO bond energies (eV) at 0 K to the experimental values

Species	Basis sets	B3LYP [a,b]	BHLYP [a,b]	MP2 [c]	CCSD(T) [c]	CCSD(T) [d]	Experiment
Th$^+$–CO	SDD/6-311+G(3df)	1.11	1.01	1.07	0.74	0.83	0.94 ± 0.06 [b]
	cc-pVTZ-PP	1.17	1.07	1.13	0.81	0.87	
	cc-pVQZ-PP	1.17	1.07	1.11	0.82	0.88	
	CBS-PP [d]	1.17	1.06	1.11	0.82	0.89	
(CO)Th$^+$–CO	SDD/6-311+G(3df)	1.10	0.93	0.93	0.83	0.94	1.05 ± 0.09
	cc-pVTZ-PP	1.14	0.97	1.00	0.89	0.98	
	cc-pVQZ-PP	1.13	0.96	1.02	0.92	1.00	
	CBS-PP [e]	1.13	0.96	1.03	0.93	1.02	

[a] All theoretical values include ZPE corrections with unscaled frequencies from structures optimized at the respective level of theory with the indicated basis set. No first-order spin-orbit corrections are needed here for (CO)Th$^+$–CO.

[b] Th$^+$–CO bond energies are from reference 29, except for B3LYP, and single point calculations at the MP2 and CCSD(T) levels, which were recalculated here.

[c] Energies from single point calculations using the B3LYP optimized structures with the indicated basis set.

[d] Th$^+$–CO bond energies are from geometry optimization and frequency calculations with the indicated basis set, from reference 29. (CO)Th$^+$–CO bond energies are from optimized geometries with the indicated basis sets, except for cc-pVQZ, which is a single point calculation using the CCSD(T)/cc-pVTZ optimized structure. ZPEs are taken from B3LYP results using the same basis set.

[e] Complete basis set limit extrapolated from cc-pVXZ (X = T and Q) basis sets as described in the text.
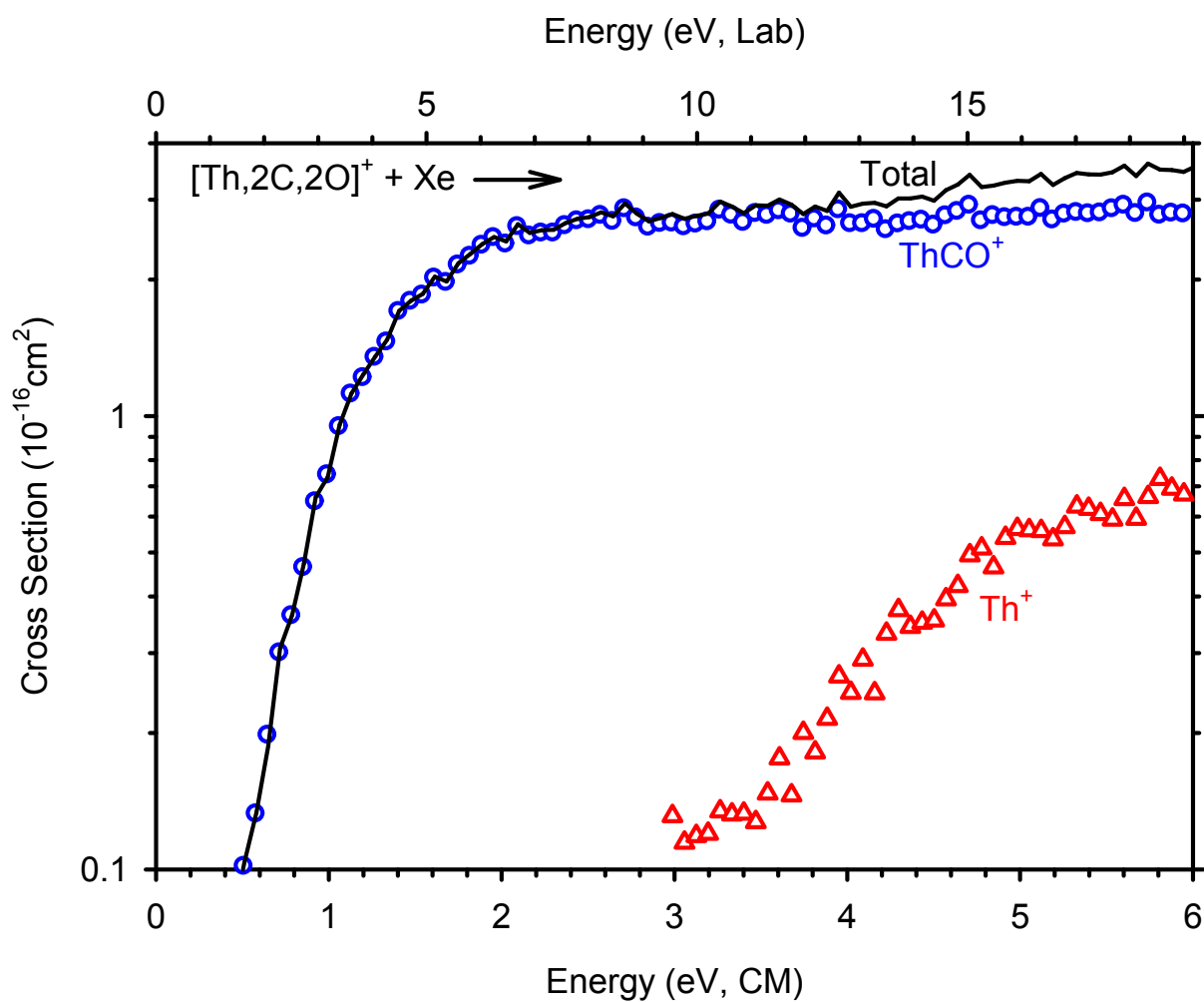
Figure 1. Cross sections for CID reactions of [Th,2C,2O]$^+$ with ~ 0.3 mTorr of Xe, as a function of kinetic energy in the center-of-mass frame (lower x-axis) and the laboratory frame (upper x-axis). Sequential loss of CO ligands occurs to form ThCO$^+$ (blue circles) and Th$^+$ (red triangles). The solid line indicates the total dissociation cross section.
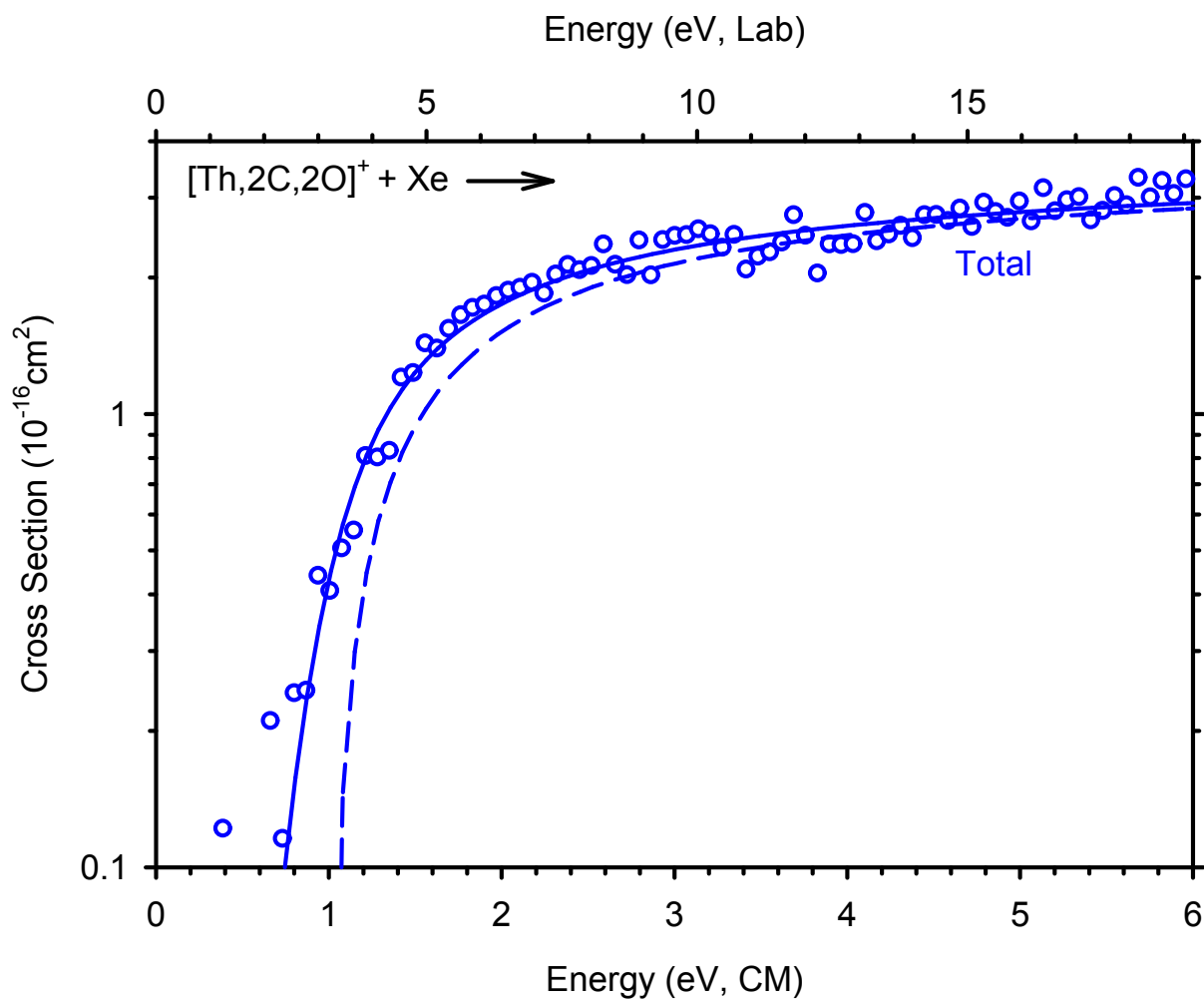
Figure 2. Zero-pressure extrapolated total dissociation cross sections (blue circles) for the CID reaction of $[Th,2C,2O]^+$ with Xe as a function of kinetic energy in the center-of-mass (lower x - axis) and laboratory (upper x-axis) frames. Blue solid (dashed) lines show the model of Eq. 1 for $Th^+(CO)_2$ reactants with (without) convolution with the internal and kinetic energy distributions of the reactants.
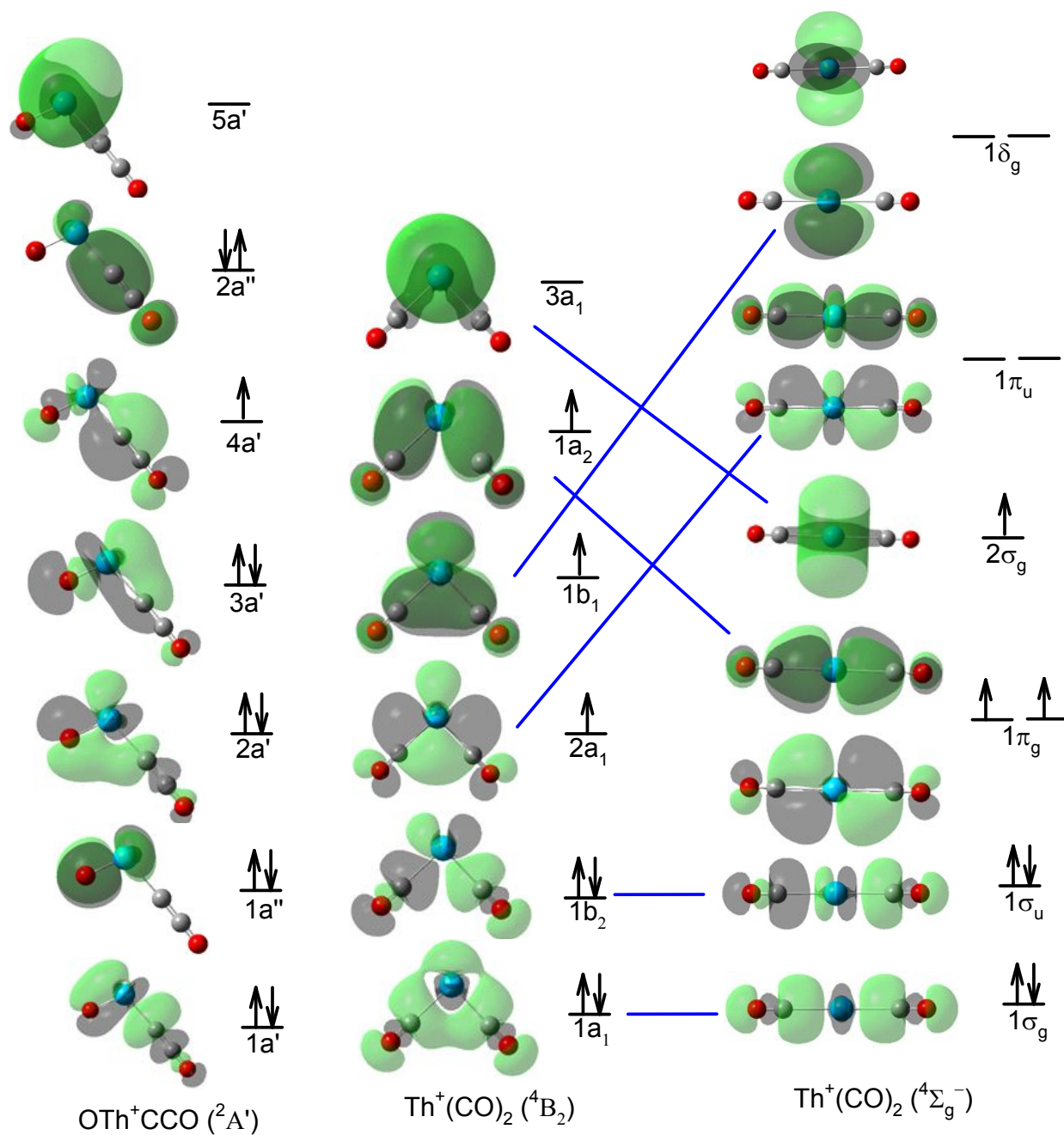
Figure 3. Valence electronic configurations and molecular orbitals for most stable states of OTh⁺CCO and bent and linear Th⁺(CO)₂ as calculated at the B3LYP/cc-pVQZ level. Th – blue, C – grey, O – red. Correlations between the MOs are shown by the blue lines.
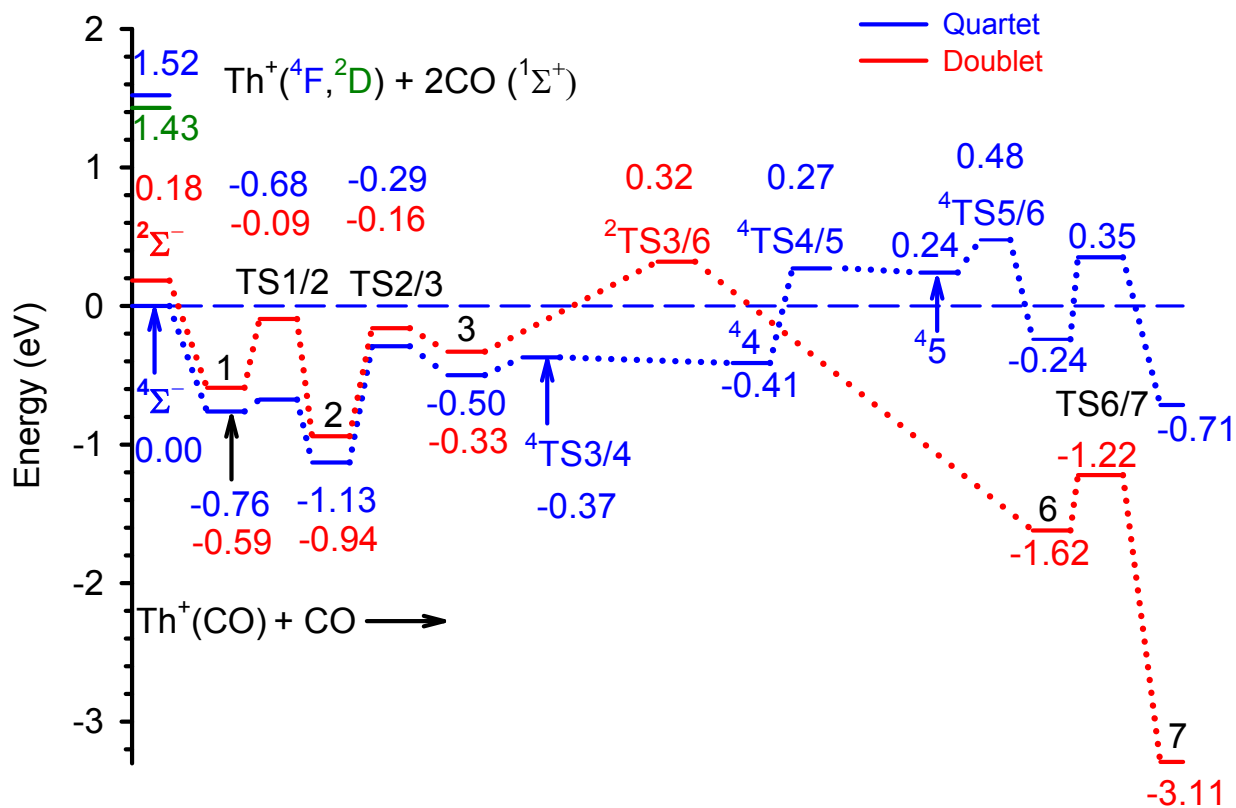
Figure 4. Potential energy profiles of [Th,2C,2O]+ for the formation of OTh+CCO calculated at the B3LYP/cc-pVQZ level for quartet (blue) and doublet (red) spins. Energies are relative to Th+(CO) ($^4\Sigma^-$) + CO. The Th+ (^{4}F, ^{2}D) + 2CO asymptotes are also given. No spin-orbit interactions are included. Structures are shown in Figure 5.
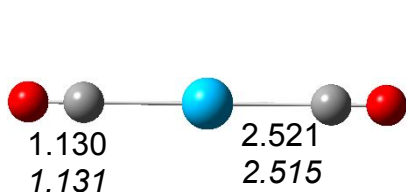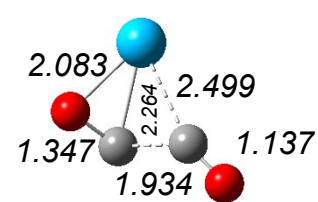
1 $Th^+(CO)_2$ ($^4\Sigma_g^-$ ($^2\Sigma_g^-$), $D_{\infty h}$)
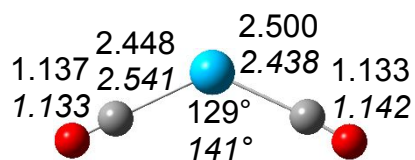
TS1/2 ($^4A''$ ($^2A'$), C_s)
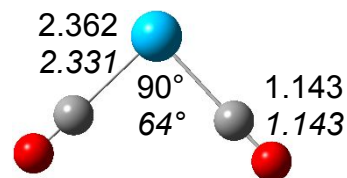
2 $Th^+(CO)_2$ ($^4B_2$ ($^2B_1$), C_{2v})
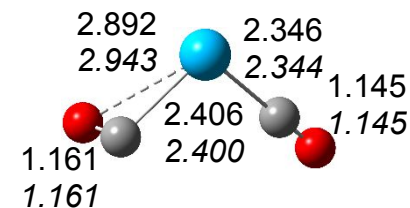
TS2/3 (^4A (^2A), C_1)
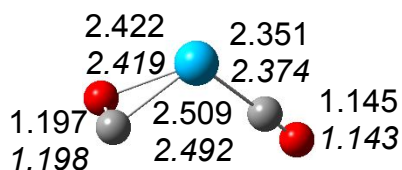
3 $OCTh^+(\eta^2$–$CO)$ (^4A (^2A), C_1)
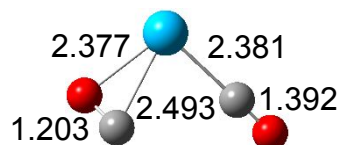
^{4}**TS3/4** (^4A, C_1)
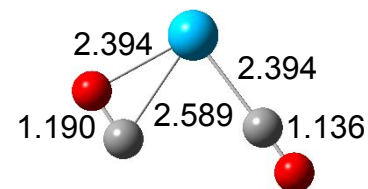
^{4}**4** $OCTh^+(\eta^2$-$CO)$ ($^4A''$, C_s)
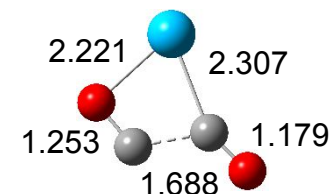
^{4}**TS4/5** ($^4A''$, C_s)
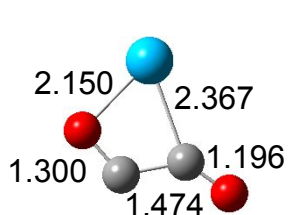
^{4}**5** $Th^+(\eta^2$–$OC(CO))$ ($^4A''$, C_s)
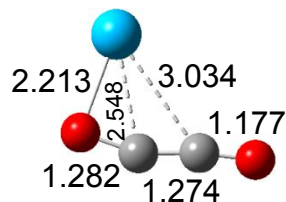
^{4}**TS5/6** ($^4A''$, C_s)

^{2}**TS3/6** (^2A, C_1)
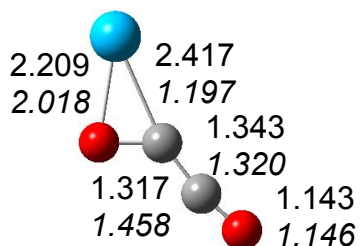
6 $Th^+(\eta^2$–$OCCO)$ ($^4A''$ ($^2A'$), C_s)
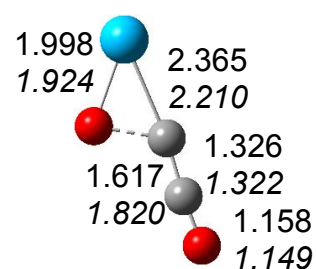
TS6/7 ($^4A''$ ($^2A'$), C_s)
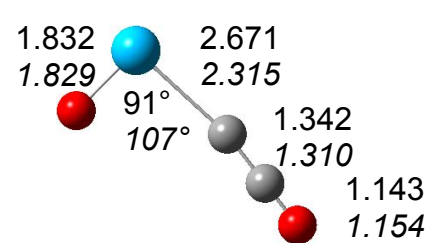
7 OTh^+CCO ($^4A''$ ($^2A'$), C_s)

Figure 5. Structures and structural parameters, bond lengths (Å) and bond angles (°), of stationary points along the [Th,2C,2O]$^+$ quartet (standard font) and doublet (italics font) potential energy profiles for the formation of OTh$^+$CCO calculated at the B3LYP/cc-pVQZ level. Th – blue, C – grey, O – red.